Enhanced optical pressure with asymmetric cavities

Yu-Chun Hsueh, Li-Fan Yang, and Kevin J. Webb

Phys. Rev. B **99**, 045437 — Published 24 January 2019

DOI: 10.1103/PhysRevB.99.045437

Enhanced Optical Pressure with Asymmetric Cavities

Yu-Chun Hsueh, Li-Fan Yang, and Kevin J. Webb*
Purdue University, West Lafayette, IN 47907, USA
* *Corresponding author: webb@purdue.edu*

Abstract

Asymmetry in a one-dimensional optical Fabry-Perot optical cavity is shown to produce a large net pressure, the total on the two mirrors. Consequently, asymmetric cavity structures that are formed in this manner can experience a net force that is greater than that resulting from the excitation light illuminating a perfect mirror. The conditions for this to occur are a modest quality factor regime, where some influence of the cavity is needed, but when the quality factor becomes very large the enhancement diminishes. This result is used to illustrate how structuring a metal surface, thereby forming a plasmonic cavity, can substantially increase the optical pressure over that possible with a planar interface. It is shown that the force on one mirror in an asymmetric arrangement can be increased relative to the other. Importantly, the sum of the pressures on both mirrors increases through asymmetry and with quality factor, while adhering to conservation of energy. Using cavity quality factor as a measure, the one-dimensional Fabry-Perot cavity pressure results are related to pressure enhancement with a structured metal surface where a different type of mode in an asymmetric cavity is excited, the lowest order metal-insulator-metal surface plasmon mode. In principle, an optical cavity or cavity array formed with any material should display this enhanced pressure phenomenon. The length scale of the resonant structures for visible light can be as small as a few tens of nanometers, in the case of metals. With this understanding guiding the design of structured metallic and dielectric materials, a many-fold increase in pressure over that on a perfect mirror is possible. Consequently, the relatively weak optical force can become more effective in a variety of scientific and technological applications.

I. INTRODUCTION

Radiation pressure was theorized [1] and measured [2, 3] more than one century ago, and optical force concepts developed since the advent of the laser have led to optical tweezers [4] and extensive interest in optical traps and condensates [5]. There has been substantial work done related to forces within optical cavities and on the cavity mirrors, primarily related to sensitivity and cooling [6–9]. Also, the development of sensitive interferometers [10] have allowed the detection of gravitational waves [11]. Generally, cavity dynamics concepts are based on the mirror radiation pressure being $P = 2\hbar k I$, with each photon carrying a momentum $\hbar k$ and I being the optical intensity measured in photons/(m^2s), given P in $\mathrm{N/m}^2$, and the factor of two is from the assumption of perfect reflection [12]. This is entirely consistent in the appropriate limit with the classical picture from Maxwell [1], where with a free space background the pressure is

$$P = \frac{S(1 + |\Gamma|^2)}{c}, \tag{1}$$

where Γ is the field reflection coefficient at the mirror, S is the time-averaged Poynting vector magnitude (the incident time-average power density), and c is the speed of light. Clearly, increasing I or the Poynting vector within the cavity by increasing the cavity quality factor (Q) will increase the pressure on each mirror. However, $|\Gamma| = 1$ leads to a maximum value of $P = 2S/c$ in this widely-held picture.

The force density in homogenized media can be obtained from the field solution, and this leads to a means to calculate the force on a medium [13, 14], the pressure on a slab [15, 16], and with photonic crystal mirrors [17]. With such an approach involving a numerical solution for the fields in the material, leading to the force density and hence pressure, the possibility of increasing the pressure by more than an order of magnitude over $2S/c$ with a nanostructured Au surface has been presented [18]. This result could be profoundly important in applications, but the physical basis of the effect has remained unclear. Here, we present an understanding based on results for an asymmetric 1D Fabry-Perot cavity and explain how the the sum of the pressures on each mirror can exceed that on a perfect mirror. This cavity mode basis leads to a means to achieve pressure enhancement with a variety of dielectric and metallic materials for remote control, propulsion, and cavity optomechanics applications. The resulting change in the mathematical picture of pressure

[1] should therefore provide a basis for new directions in optomechanics for the physical sciences.

We explain optical pressure enhancement on a surface by considering the mirror pressures in the 1D Fabry-Perot cavities shown in Figs. 1(a) and (b), which we relate to cavity Q and the metal-insulator-metal (MIM) cavity mode in Figs. 1(c) and (d), all in a free space background. Figure 1(a) shows a symmetric cavity containing two identical slab mirrors (M_1 and M_2) with thickness t, and a cavity length d, defined as the mirror separation. Figure 1(b) shows an asymmetric cavity with M_1 having thickness t and the semi-infinite M_2 placed a distance d away from M_1. Figure 1(c) shows a nanostructured slot cavity array in metal and the profile of each slot is shown in Fig. 1(d). With an incident field having H_z, the lowest order MIM waveguide mode (E_x, E_y, H_z) can be excited, by virtue of the metal dielectric constant ($\epsilon = \epsilon' + i\epsilon''$ with $\epsilon' < -1$, assuming a free space background) [19]. The coupled surface plasmon waveguide mode has a wavelength that reduces with decreasing slot width (Σ), allowing for resonant cavities in gold (Au) where the slot depth (D) and Σ are just a few tens of nanometers. The cavity in Fig. 1(d) has differing reflection coefficients at the top and bottom of the slot, resulting in asymmetry. We present radiation pressure simulation results for 1D cavities in Figs. 1(a) and (b) and use these to build physical insight into the influence of structures like Figs. 1(c) and (d) to enhance the pressure.

II. ASYMMETRIC CAVITY PRESSURE

The separable problems in Figs. 1(a) and (b) can be solved analytically, and we do so for excitation with a single, normally incident plane wave from the left, allowing the force densities in the mirrors and hence the pressure to be obtained. Using impedance transformation, the field reflection coefficient, S_{11} (with scattering parameter notation), can be found at the left interface of M_1 [20]. We choose reflected fields rather than those transmitted because some cavities of interest have no transmission. Using the recursive from of the field transmission matrix, the fields are found in the cavity and within the mirrors [20]. The fields in the mirrors lead to the force density and hence the pressure. The force density expression we utilize here, originally from Einstein and Laub [21], has been derived and used by others [13, 14, 16, 22], and was also used to present the idea of enhanced pressure in structured material [18]. We assume that no magnetic material response exists in the source-free case. Consequently, the time-averaged force density within the material media assuming $\exp(-i\omega t)$ is

$$\langle \mathbf{f} \rangle = (\hat{\mathbf{e}} \times \hat{\mathbf{h}}) \frac{\mu_0 \epsilon_0 \omega}{2} \Im\{\chi_E E(\mathbf{r}) H^*(\mathbf{r})\} + \frac{\epsilon_0}{2} \Re\{(\chi_E E(\mathbf{r}) \hat{\mathbf{e}} \cdot \nabla)(\hat{\mathbf{e}} E^*(\mathbf{r}))\}, \tag{2}$$

where $\hat{\mathbf{e}}$ and $\hat{\mathbf{h}}$ are unit vectors indicating the direction of the electric and magnetic field phasors, E and H, at position $\mathbf{r}$, respectively, χ_E is the electric susceptibility, $\Re\{\cdot\}$ is the real part and $\Im\{\cdot\}$ the imaginary part, μ_0 is the free space permeability, and ϵ_0 is the free space permittivity. We define the time-averaged force density due to the first term in (2) as $\langle \mathbf{f}_\mathrm{R} \rangle$, where the nomenclature implies that this is the radiation pressure for a planar surface with normal incidence, the usual mirror picture, and the other term due to the gradient of the field as $\langle \mathbf{f}_\mathrm{G} \rangle$. We note that application of (2) for normally incident light on a planar Au mirror and integration over depth produces a pressure for visible wavelengths that is very close to $2S/c$. Conservation of momentum is inherent in use of (2) because this kinetic force density is formed with use of the classical field momentum [13, 21, 23].

We relate the radiation pressure to the cavity Q for the 1D cavities in Figs. 1(a) and (b). With the linear and isotropic relationships $\mathbf{D} = \epsilon_0 \epsilon \mathbf{E}$ and $\mathbf{B} = \mu_0 \mathbf{H}$, in frequency domain and where $\mathbf{D}$ is the electric flux density and $\mathbf{B}$ the magnetic flux density, it is possible to separate electromagnetic field energy into stored and lost components [24]. Under the assumption that dispersion can be neglected, so $\partial \epsilon / \partial \omega = 0$, the time-averaged stored energy surface density (J/m^2) is

$$W = \frac{1}{4} \int_l \left[\epsilon' \epsilon_0 |E(\mathbf{r})|^2 + \mu_0 |H(\mathbf{r})|^2 \right] \mathrm{d}l, \tag{3}$$

where l is the spatial variable perpendicular to the mirrors. Likewise, the time-averaged power dissipation surface density (W/m^2) is

$$P_\mathrm{d} = \frac{\omega}{2} \int_l \epsilon_0 \epsilon'' |E(\mathbf{r})|^2 \mathrm{d}l. \tag{4}$$

The integrations in (3) and (4) are over the mirrors and the intervening space (free space in the situations of Figs. 1(a) and (b)), and for M_2 in the asymmetric cavity case, the integral in that mirror is over 20δ, with δ the skin depth (e^{-1} of the field at the surface).

The Q can be decomposed into unloaded (accounting for loss within the cavity, Q_U) and loaded (describing the radiative loss contribution, Q_L) as

$$\frac{1}{Q} = \frac{1}{Q_\mathrm{U}} + \frac{1}{Q_\mathrm{L}}, \tag{5}$$

where

$$Q_{\mathrm{U}} = \omega_0 \frac{W_0}{P_{\mathrm{d}}} \quad \text{and} \quad Q_{\mathrm{L}} = \omega_0 \frac{W_0}{S_{\mathrm{r}} + S_{\mathrm{t}}}, \tag{6}$$

with ω_0 the resonant circular frequency, W_0 the total (electric plus magnetic) energy in the cavity at resonance from (3), P_{d} the power dissipated within the cavity at resonance from (4), and S_{r} and S_{t} the reflected and transmitted Poynting vector magnitudes, respectively, at resonance. With high cavity finesse and use of a Lorentzian line model [25, 26],

$$1 - |S_{11}(\omega)|^2 = \frac{1 - |S_{11}(\omega_0)|^2}{1 + 4\frac{(\omega_0 - \omega)^2}{\Delta\omega^2}}, \tag{7}$$

and an estimate of Q is

$$Q_\omega = \frac{\omega_0}{\Delta\omega}, \tag{8}$$

where $\Delta\omega$ is the half-power bandwidth and the subscript ω indicates this frequency response measure (with a high Q approximation). Measuring S_{11} and use of (8) to determine Q circumvents the need to artificially define cavity boundaries.

III. PRESSURE WITH A ONE-DIMENSIONAL ASYMMETRIC CAVITY

Figure 2 shows our pressure results for the 1D cavities of Figs. 1(a) and (b) at resonance. We designate symmetric (Fig. 1(a)) and asymmetric (Fig. 1(b)) Fabry-Perot cavity cases through the labels SFP and AFP, respectively. In all calculations, the magnitude of the Poynting vector of the normally incident plane wave (S_i) on the cavity is 1 W/m^2, and the free space wavelength is $\lambda_0 = 633$ nm. The mirror dielectric constants used are presented in Table I and based on Au. We vary only the material loss and thickness to adjust the confinement and dissipation in the cavities. The shortest resonant cavity length was determined from the minimum $|S_{11}|$ as d is adjusted, and all results are for this condition. For the 1D cavities, only $\langle \mathbf{f}_{\mathrm{R}} \rangle$ contributes to the pressure. Positive pressure is in the direction of the wave vector for the cavity excitation and the excitation Poynting vector. Consequently, M_1 has positive pressure due to excitation and negative pressure due to the cavity field, and the latter dominates in the cases considered. The pressure on M_2 is always positive. Our central interest is in the sum of the pressures on the two mirrors.

Figure 2(a) shows the radiation pressure on M_2, P_{M_2}, as a function of Q, calculated from (5), with use of (6), and the cavity energy determined from (3) and the power dissipation from (4). The various symmetric (SFP) and asymmetric (AFP) cavity parameters are given in Table I. The Q is adjusted by varying the loss in M_1 through $\epsilon''_{\mathrm{M}_1}$. Changing $\epsilon''_{\mathrm{M}_1}$ has an impact on the coupling between the incident wave and the cavity, so both Q_{U} and Q_{L} are varied, and the stored energy in the cavity changes. The increase in P_{M_2} with increasing Q can be understood from the pressure presented by Maxwell [1] in (1) with $|\Gamma| \sim 1$ and the increasing forward power density (S_{f}). A fit (orange line) in Fig. 2(a) makes the linear relationship between pressure and Q clear. Figure 2(b) shows P_{M_2} as a function of Q_ω, estimated from (8), which has a nonlinear relationship to pressure. However, the general trend between pressure and both Q and Q_ω are consistent. The nonlinear character in Fig. 2(b) appears at lower values of Q_ω and can be attributed to the breakdown of the high-Q approximation. With high Q_ω, the results in Fig. 2(b) still differ a little from those in Fig. 2(a) because the cavity boundaries were (artificially) described at the outside of the mirror surfaces in determining both W_0 and Q (in Fig. 2(a)), while use of the reflection coefficient in (7) in determining Q_ω from (8) did not require a cavity boundary to be defined. We conclude then that Q_ω provides a suitable measure to investigate cavity mirror pressure.

Figure 2(c) shows the net pressure on M_1 and M_2, $P_{\mathrm{M}_1} + P_{\mathrm{M}_2} = P_{\mathrm{M}_1+\mathrm{M}_2}$, for SFP2 and AFP3, the higher Q examples of symmetric and asymmetric cavities, respectively. When a symmetric cavity is resonant, the forward and backward waves within the cavity have approximately the same amplitude. Therefore, for the symmetric cavity, P_{M_1} (< 0, the sum of the excitation light pressure, which is positive, and the much larger negative cavity pressure) is almost the same as P_{M_2} (> 0), but in the opposite direction and hence a negative number, causing $P_{\mathrm{M}_1+\mathrm{M}_2}$ to be small. This can be observed from the blue diamond symbols in Fig. 2(c), where the total pressure becomes small as Q_ω increases. On the other hand, with the asymmetric mirror arrangement of Fig. 1(b), P_{M_2} is slightly larger than P_{M_1}, leading to an increasing $P_{\mathrm{M}_1+\mathrm{M}_2}$ with increase in Q_ω over the range considered, as evidenced by the star symbols in Fig. 2(c). The dashed line in Fig. 2(c) shows the maximum pressure on a perfect mirror based on (1) when $S = 1\ \mathrm{W/m^2}$ and $\Gamma = 1$. From the AFP3 case in Fig. 2(c), given by the blue stars, it is clear that $P_{\mathrm{M}_1+\mathrm{M}_2}$, enhanced by the cavity Q, can exceed the maximum pressure on a perfect mirror ($2S/c$) by a factor of three (with the same power density incident on the cavity).

Figure 2(d) shows the power flow for the asymmetric cavity case of Fig. 2(c), AFP3. Conservation of energy requires that the difference between the forward and backward Poynting vector magnitudes in the cavity and between the mirrors ($S_\mathrm{f} - S_\mathrm{b}$) be less than or equal to (when the mirrors have no dissipative loss) the net power density exciting the cavity ($S_\mathrm{i} - S_\mathrm{r}$). Figure 2(d) shows that this is the case and energy is conserved. The $S_\mathrm{f} - S_\mathrm{b}$ curve approaches $S_\mathrm{i} - S_\mathrm{r}$ with increasing Q because the loss in M_1 is being reduced. We can thus understand the enhanced net pressure ($P_{\mathrm{M}_1+\mathrm{M}_2}$) as being regulated by asymmetric cavity control of $S_\mathrm{f} - S_\mathrm{b}$ and cavity Q, while maintaining conservation of energy and momentum.

It is interesting to note from the asymmetric cavity results of Fig. 2 that, at the first resonance, $P_{\mathrm{M}_1+\mathrm{M}_2}$ is largest when the reflection coefficient at the left of M_1 ($|S_{11}|$) is a minimum. On the contrary, the maximum pressure based upon $S(1 + |\Gamma|^2)/c = 2S/c$ occurs when the reflection coefficient is maximum. The idea that higher reflection produces larger pressure has led to the use of highly reflecting surfaces achieved with distributed Bragg reflectors or photonic crystals. Our results indicate, quite differently, that a resonant asymmetric cavity can provide even larger pressure enhancement than the conventional limit.

To understand the pressure enhancement when the cavity supports even higher Q, we calculate the net pressure, $P_{\mathrm{M}_1+\mathrm{M}_2}$, for symmetric and asymmetric Fabry-Perot cavities with Q_ω larger than AFP3 in Fig. 2(c), finding the results in Fig. 3(a). The dielectric constants of M_1 and M_2 are fixed to be $\epsilon'_{\mathrm{M1}} = \epsilon'_{\mathrm{M2}} = -11.82$ and $\epsilon''_{\mathrm{M1}} = \epsilon''_{\mathrm{M2}} = 0.1$. We adjust the thickness of M_1, t, to be $5, 10, 40, 50, 70, 80, 100, 130$ and 150 nm to gradually increase cavity quality factor, Q_ω. The symmetric cavities have identical thicknesses for M_1 and M_2. In principle, the symmetric cavity pressure should approach the perfect mirror case, the dashed line in Fig. 2(c), when M_1 is very thick, to obtain high Q. This can be observed from the diamond symbols. Note how $P_{\mathrm{M}_1+\mathrm{M}_2}$ increases to approach the dashed line and the perfect mirror situation, indicating that the internal cavity pressures cancel and the small cavity coupling results in close to a perfect mirror for the excitation field at M_1. For the asymmetric cavities (star symbols), notice in Fig. 3(a) that $P_{\mathrm{M}_1+\mathrm{M}_2}$ has a value below the perfect mirror case and initially increases with increasing Q_ω, reaches a maximum, and then decreases to the perfect mirror value. When t becomes large and cavity Q is very high, the cavity behaves more like a symmetric cavity where the pressures on M_1 and M_2 due to S_b and S_f cancel. The net pressure for high Q approaches that from the excitation wave on a planar surface. We therefore learn by way of example and consideration of the underlying physical mechanism that there is a regime with modestly high Q where pressure enhancement with asymmetric cavities can occur.

IV. CAVITY PRESSURE WITH MAXWELL'S PICTURE

In Fig. 2 we show calculated results for the pressure from a force density stemming from work by Einstein and Laub [21] given in (2). Integration of the force density over the material and normalization to surface area led to the pressure. For the 1D cavity problem we treated and normal incidence, only the first term in (2) contributes. On the other hand, a commonly used picture was proposed by Maxwell [1], where the radiation pressure is given by (1) when there is no transmission through the mirror.

We compare the pressures on M_1 and M_2 in Fig. 1(b), P_{M1} and P_{M2}, based on these two approaches, i.e., with use of (1) and (2). In applying (1) to M_1, we consider only the more significant pressure from the cavity field and hence neglect that due to the excitation field on this mirror. We choose AFP3 (the asymmetric cavity in Fig. 1(b) with the parameters given in Table I) because of the larger pressure enhancement and higher Q among the Fabry-Perot cavity examples in Fig. 2. The results for P_{M1}, P_{M2} and the net pressure, $P_{\mathrm{M1+M2}}$, for AFP3, are shown in Fig. 4. Changing the material in mirror M_1 produces a change in cavity Q and hence a change in the pressure. In Fig. 4, the black stars are from Maxwell's picture in (1) and the blue stars are calculated from (2).

We note that P_{M1} is in the opposite direction of P_{M2}. By using (1) for P_{M1}, we assume that M_1 provides high reflection and efficient absorption within the material. Therefore, the results have the assumption that no transmission occurs through M_1, causing a slightly larger P_{M1}. We can also observe the slight differences between the pressures calculated from two approaches in Fig. 4(b) due to the influence of the finite penetration (20δ, with δ the skin depth) into M_2 in forming the pressure from (2). These small differences are more evident for larger Q_ω because the scale is expanded in this regime and reduce with increasing accuracy for the integration of the force density. The use of (1) for M_1 produces higher P_{M1} and hence a lower estimate for the net pressure, $P_{\mathrm{M1+M2}}$. This can be observed in Fig. 4(c) with increasing Q_ω. With an increase of Q_ω, the loss of M_1 reduces, causing the larger differences between the two approaches when we use (1) for M_1. However, the enhanced pressure beyond that on a perfect mirror can still be observed when we apply Maxwell's picture. Generally, for this 1D problem, we note the excellent agreement between the two approaches. Our conclusion is that either model would serve our purpose.

To confirm that we have the correct field solutions, Fig. 5 plots the magnitudes of the electric and magnetic fields through the cavity for the three AFP3 examples with the largest Q ($Q_\omega = 135.84, 120, 107.67$ when $\epsilon''_{\mathrm{M}_1} = 0, 0.1, 0.2$, respectively) in Fig. 4 where there is significant pressure enhancement and high Q. The field values can be used to verify the corresponding power flow points in Fig. 2(d) and the pressure enhancement for this case. The magnitude of electric field in Fig. 5(a), (c) and (e) and magnetic field in Fig. 5(b), (d) and (f) indicate the quasi-even electric field and quasi-odd magnetic field solutions for the first resonant mode in the asymmetric cavity. These field solutions clearly satisfy the boundary conditions and hence represent both the unique and exact field solution for this particular situation. Consequently, the approximate pressures from (1) or the exact results from (2) presented in Fig. 4(c) can be verified. We provide the numbers for power flow, S_{f} and S_{b}, and the reflection coefficients at M_1 and M_2, $|\Gamma_1|^2$ and $|\Gamma_2|^2$, in the caption of Fig. 5, and these produce the corresponding pressure points in Fig. 4.

V. ANALYTICAL DESCRIPTION OF ENHANCED CAVITY PRESSURE

Equation (1) provides a simple, approximate means to develop an analytical pressure expression for the 1D cavity. We assume a backward power flow in the cavity given by

$$S_b = \alpha Q S_i, \tag{9}$$

where α is a constant that relates Q to Poynting vector magnitude. Upon neglecting the influence of the transmission through Mirror 1 on pressure and assuming high Q, such that the pressure due to the excitation light on Mirror 1 can be neglected, (1) yields

$$\begin{aligned} P_{\mathrm{M}_1} &= -\frac{S_b}{c}\left(1 + |\Gamma_1|^2\right) && (10)\\ &= -\frac{\alpha Q S_i}{c}\left(1 + |\Gamma_1|^2\right). && (11)\end{aligned}$$

Similarly, the pressure on M_2 can be written as

$$P_{\mathrm{M}_2} = \frac{\alpha Q S_i}{c}\left(1 + |\Gamma_2|^2\right). \tag{12}$$

Summing (11) and (12), we have

$$P_{\mathrm{M}_1+\mathrm{M}_2} = \frac{\alpha Q S_i}{c}\left[|\Gamma_2|^2 - |\Gamma_1|^2\right]. \tag{13}$$

Consider the case of an asymmetric cavity where $|\Gamma_2| = 1$, so (13) becomes

$$P_{\mathrm{M}_1+\mathrm{M}_2} = \frac{S_i}{c}\alpha Q\left[1 - |\Gamma_1|^2\right]. \tag{14}$$

We note that $\Gamma_1 = f(Q)$ is smooth but nonlinear. This facilitates a local, linear approximation for a range of Q and hence a simple means to incorporate this dependence into (14). Referring to (14), we set $\gamma = 1 - |\Gamma_1|^2$ and use the local linear relationship

$$Q = a\gamma + b. \tag{15}$$

Substituting $1 - |\Gamma_1|^2 = \gamma = (Q - b)/a$ into (14), we have

$$P_{\mathrm{M}_1+\mathrm{M}_2} = \frac{\alpha S_i Q}{ac}\left[Q - b\right], \tag{16}$$

a quadratic equation in Q.

Using this simple, analytical picture, we can gain insight into the enhanced pressure regime in Fig. 3(a) and where the maximum $P_{\mathrm{M}_1+\mathrm{M}_2}$ occurs. Equation (16) assumes $|\Gamma_2|^2 = 1$ and AFP3 in Fig. 2(a) uses $|\Gamma_2|^2 = 0.9955 \approx 1$. Therefore, we can use Fig. 2(a) to find Q and hence α in (12). This procedure yields $\alpha = 0.2027$. Because we calculate Q_ω and (16) is a function of Q, we use the asymmetric cavity data point with $t = 50$ nm, which shows the largest pressure enhancement in Fig. 3(a), to relate Q_ω to Q by $Q = \beta Q_\omega$. Note that this point is also the one in AFP3 with the second largest Q (blue star in Fig.2(a)). Therefore, with use of Fig. 2(a), we find $\beta = 2.6073$. We then write

$$\begin{aligned} Q_\omega &= \frac{1}{\beta}\left(a\gamma + b\right) \qquad (17) \\ &= a_n\gamma + b_n, \qquad (18) \end{aligned}$$

where $a_n = a/\beta$ and $b_n = b/\beta$.

Figure 3(b) shows calculated points ($t = 40, 50, 70$ and 80 nm) for Q_ω as a function of $\gamma = 1 - |\Gamma_1|^2$. The blue line in Fig. 3(b) is the least mean-square error fit to the points and is selected as a line to determine $Q_\omega = a_n\gamma + b_n$. We thus obtained the parameters $a_n < 0$ and $b_n > 0$ in (16), with $a_n = -4.5350 \times 10^3$ and $b_n = 407.3813$. Equation (16) with either Q or Q_ω, related by $Q = \beta Q_\omega$, can thus be used to find the local approximation to $P_{\mathrm{M}_1+\mathrm{M}_2}$, and this is the (red) parabola plotted in Fig. 3(a). The local maximum of the enhancement occurs when Q_ω is around 200. Notice that this simple, locally linear description nicely captures the essence of the pressure enhancement. A series of such local solutions will provide the set of perturbational solutions.

VI. PRESSURE WITH A SLOT ARRAY IN A METAL FILM

To obtain the fields and the corresponding radiation pressure in the nanostructured slot cavity in a metal film, shown in Fig. 1(c), we use a frequency domain finite element method (FEM) to obtain the numerical field solutions [27]. Port boundaries are used in this 2-D model to extract S_{11} and placed $5\lambda_0$ above and below the structure in Fig. 1(d). To avoid singularities in the numerical simulations, the corners of each slot are rounded with radius of 1 nm. The maximum mesh element size in the scattering material is $\lambda_0/200$, sufficient to ensure the accuracy of the force density solutions. The slot depth, D, and width, Σ, are variables and the period is set to $\Lambda = 400$ nm and thickness to $T = 200$ nm. With a period of $\Lambda = 400$ nm, only the zeroth-order (normal) scattered plane wave propagates. We fix Σ and vary D to determine the resonant depth from the minimum of $|S_{11}|$.

The results for the slot resonant D as a function of Σ, labeled by the (red) diamonds, are shown on the right axes in Figs. 6(a) and (b). A reducing slot width results in a decreasing slot depth for the first resonance. We apply (8) to estimate Q_ω for the slot cavity, and the results are shown in Fig. 6(a) by the (black) triangles in conjunction with the left axis. Note that Q_ω increases with decreasing Σ, which can be understood by the cavity reflection coefficient at the top of the slot increasing as Σ is reduced, thereby increasing the lifetime of the guided-wave resonance in the slot and hence Q_L. The numerical field solutions are used in (2) to find the force density, and this is integrated over the support of the material within the unit cell and divided by Λ to form the pressure, with the results given by the (black) asterisks for each value of Σ in Fig. 6(b), as indicated on the left axis. The general trends in Figs. 6(a) and (b) are that both Q_ω and pressure decrease with increasing slot width (at resonance). The pressure results for the slot cavities in Fig. 6(b) are consistent with the asymmetric 1D Fabry-Perot cavity results of Fig. 2(c) for AFP3, where the pressure increases with Q_ω. The anomalous pressure result for the smallest Σ in Fig. 6(b) occurs because of the small slot size and the reduced interaction between the field and the material. Figure 6(c) shows the pressure as a function of Q_ω for the slot structures. Unlike the 1D Fabry-Perot cavities, the gradient force term, $\langle \mathbf{f}_{\mathrm{G}} \rangle$, contributes. We separate the contribution of $\langle \mathbf{f}_{\mathrm{G}} \rangle$ from the total pressure (black asterisks), and the results are plotted as the red circles in Fig. 6(c). In general, the pressure is proportional to Q_ω and the relationship is linear for lower Q_ω. Higher Q_ω supports a higher pressure contribution from $\langle \mathbf{f}_{\mathrm{G}} \rangle$, associated with the reducing slot width, although the total pressure reduces slightly at the highest Q_ω. The dashed line is again the maximum pressure on a perfect mirror, from Fig. 2(c). Compared to the net pressure for the AFP3 1D cavity case in Fig. 2(d), the slot cavity can provide a pressure enhancement more than an order of magnitude higher than a perfect mirror with a relatively low-Q cavity. The gradient of the total pressure in Fig. 6(c), dP/dQ_ω, describes the efficacy of the cavity in enhancing the pressure (per unit Q or stored energy). In Fig. 6(d), we plot the linear fits passing through the origin for the total pressure and the pressure contributed by $\langle \mathbf{f}_\mathrm{G} \rangle$ as black and red dashed lines, respectively, using the first 8 points (linear region) in Fig. 6(c). Linear fits to the pressure as a function of Q_ω for SFP1 and AFP1, which involve similar (low) Q_ω to the slot cavity, are plotted for comparison as the red and blue lines, respectively, in Fig. 6(d). The nanostructured slot cavity can provide larger pressure enhancement on the target surface than that (on M_2) for the 1D Fabry-Perot cavities we considered when the cavities have the same Q. This is mainly due to the contribution of the gradient force, $\langle \mathbf{f}_\mathrm{G} \rangle$. Consequently, for an incident wave with time-averaged intensity S, the nanostructured slot cavity can utilize the energy stored in the cavity more efficiently in creating optomechanical pressure by drawing on both $\langle \mathbf{f}_\mathrm{R} \rangle$ and $\langle \mathbf{f}_\mathrm{G} \rangle$.

VII. CONCLUSION

We have shown that an asymmetric optical cavity can lead to a total pressure as the sum of that on each mirror that exceeds the pressure on a perfect mirror. This net pressure is substantial by virtue of the asymmetry and can be controlled by cavity Q. The enhanced pressure for the nanostructured metal film results from both terms in (2), where the cavity mode resonance influences the fields in the metal and hence the force density and pressure. Generally, increasing the cavity Q can produce higher pressure in the metal film slot resonators. The kinetic force density in (2) is derived using conservation of momentum (see [13], for example). Consequently, there is a rigorous basis for the pressure results shown.

The 1D cavity provides a simple vehicle to understand enhanced optical pressure, defined as the sum of the pressure on both mirrors in a Fabry-Perot cavity. With planar mirrors and the neglection of transmission, the simple pressure description from Maxwell in (1) holds and provides a useful comparison and the basis for a mathematical picture of pressure enhancement. We have provided a rigorous physical and mathematical pressure development and results. However, there is a consistent qualitative picture. Conservation of energy has been demonstrated in our results (Fig. 2(d)). The large cavity fields and power flow imply an accumulation of photons and a larger number of photons per unit time striking the interior walls of the cavity than is the case for the external mirror surface through which excitation occurred. The cavity could have been populated with photons by some other means, such as an internal source. Regardless, with appreciable cavity field enhancement, the pressures from inside dominates. With the introduction of asymmetry in the cavity mirrors, the pressure on one mirror can exceed the other by an amount that is greater than the equivalent excitation light applied to a perfect, planar mirror (Fig. 2(c) and Fig. 3(a)). As we have shown, this can occur with satisfaction of energy and momentum conservation.

A surface plasmon is excited in the slot cavity in a metal film described, associated with the lowest-order MIM mode that propagates for arbitrarily small slot width, allowing for very small cavities. However, other cavity modes using other materials, including dielectrics, are expected to also provide pressure enhancement. This is illustrated in the 1D cavity results we showed, where a surface plasmon was not excited in the metal-like mirrors, and these could have been replaced with dielectric counterparts with similar results.

There are convenient fabrication methods to form nanocavity arrays in metal, for example, direct nanoimprinting [28]. With use of optimized, aperiodic structures, more control and higher pressure should be possible [29], and regulation of the pressure as a function of wavelength should be possible. The explanation for enhancement we have provided allows design guidelines for applications that will benefit from enhanced and controllable optical forces with structured material. For example, beads that are used in optical tweezers could be structured [30]. Also, the efficacy of vehicle propulsion using structured materials should improve. More generally, we suggest that there are new opportunities related to the interaction of waves with structured, resonant materials and the generation of a mechanical response.

VIII. ACKNOWLEDGMENTS

This work was supported by the Air Force Office of Scientific Research (FA9550-16-1-0064) and the Army Research Office (W911NF1610359).

---

[1] J. C. Maxwell, *A Treatise on Electricity and Magnetism*, Vol. 1 (Clarendon press, 1881).

[2] P. Lebedev, Ann. Phys **6**, 433 (1901).

[3] E. F. Nichols and G. F. Hull, Phys. Rev. **17**, 26 (1903).

[4] A. Ashkin, J. M. Dziedzic, J. E. Bjorkholm, and S. Chu, Opt. Lett. **11**, 288 (1986).

[5] D. J. Wineland and W. M. Itano, Phys. Rev. A **20**, 1521 (1979).

[6] V. B. Braginski and A. B. Manukin, Sov. Phys. JETP **25**, 653 (1967).

[7] A. Dorsel, J. D. McCullen, P. Meystre, E. Vignes, and H. Walther, Phys. Rev. Lett. **51**, 1550 (1983).

[8] T. J. Kippenberg, H. Rokhsari, T. Carmon, A. Scherer, and K. J. Vahala, Phys. Rev. Lett. **95**, 033901 (2005).

[9] S. Gigan, H. R. Böhm, M. Paternostro, F. Blaser, G. Langer, J. B. Hertzberg, K. C. Schwab, D. Bäuerle, M. Aspelmeyer, and A. Zeilinger, Nature **444**, 67 (2006).

[10] A. Abramovici, W. E. Althouse, R. W. Drever, Y. Gürsel, S. Kawamura, F. J. Raab, D. Shoemaker, L. Sievers, R. E. Spero, K. S. Thorne, R. E. Vogt, R. Weiss, S. E. Whitcomb, and M. E. Zucker, Science **256**, 325 (1992).

[11] B. P. Abbott, R. Abbott, T. D. Abbott, M. Abernathy, F. Acernese, K. Ackley, C. Adams, T. Adams, P. Addesso, R. X. Adhikari, *et al.*, Phys. Rev. Lett. **116**, 061102 (2016).

[12] O. Arcizet, T. Briant, A. Heidmann, and M. Pinard, Phys. Rev. A **73**, 033819 (2006).

[13] K. J. Webb and Shivanand, Phys. Rev. E **84**, 057602 (2011).

[14] M. Mansuripur, A. R. Zakharian, and E. M. Wright, Phys. Rev. A **88**, 023826 (2013).

[15] A. Mizrahi and L. Schächter, Phys. Rev. E **74**, 036504 (2006).

[16] Shivanand and K. J. Webb, J. Opt. Soc. Am. B **29**, 3330 (2012).

[17] M. I. Antonoyiannakis and J. B. Pendry, Phys. Rev. B **60**, 2363 (1999).

[18] A. H. Velzen and K. J. Webb, Phys. Rev. B **92**, 115416 (2015).

[19] K. J. Webb and J. Li, Phys. Rev. B **73**, 033401 (2006).

[20] Please refer to Supplemental Material for details.

[21] A. Einstein and J. Laub, Ann. Phys. **331**, 541 (1908).

[22] P. Penfield and H. A. Haus, *Electrodynamics of Moving Media* (MIT Press, Cambridge, MA, 1967).

[23] K. J. Webb, Phys. Rev. Lett. **111**, 043602 (2013).

[24] K. J. Webb and Shivanand, J. Opt. Soc. Am. B **27**, 1215 (2010).

[25] M. C. Sanchez, E. Martin, and J. M. Zamarro, in *Proc. Inst. Elect. Eng., pt. H*, Vol. 137 (IET, 1990) pp. 209–212.

[26] P. J. Petersan and S. M. Anlage, J. Appl. Phys. **84**, 3392 (1998).

[27] COMSOL, "Comsol multiphysics modeling software," `http://www.comsol.com`.

[28] S. Kim, Y. Xuan, V. P. Drachev, L. T. Varghese, L. Fan, M. Qi, and K. J. Webb, Opt. Express **21**, 15081 (2013).

[29] Y.-C. Hsueh and K. J. Webb, J. Opt. Soc. Am. B **34**, 2059 (2017).

[30] J. R. Moffitt, Y. R. Chemla, S. B. Smith, and C. Bustamante, Annu. Rev. Biochem. **77**, 205 (2008).

FIGURES

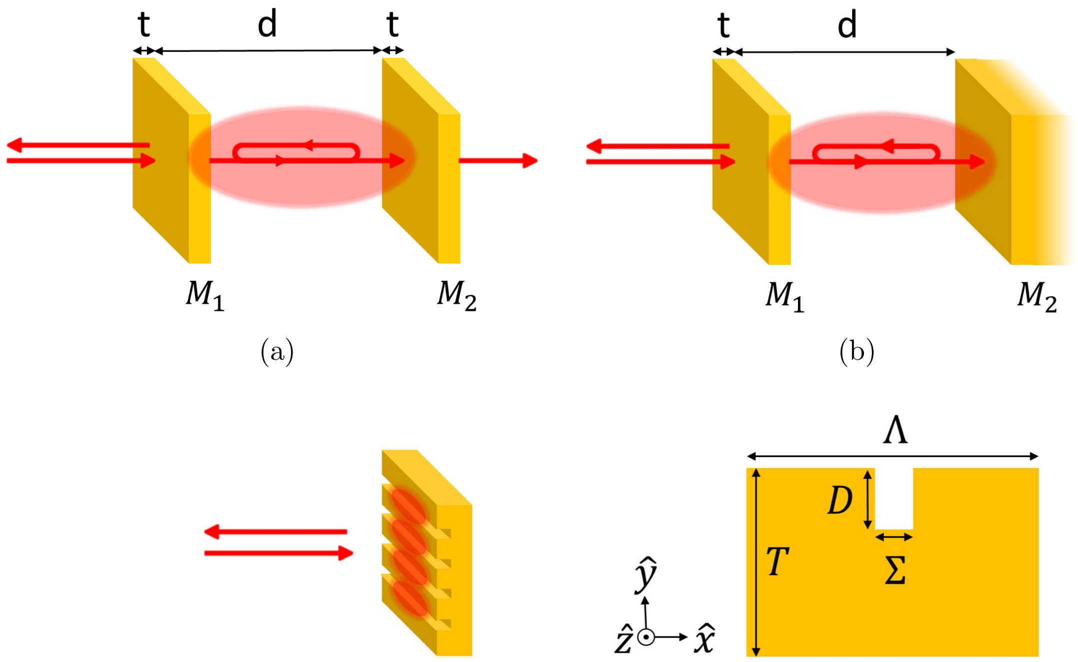

(a) (b)

(c) (d)

FIG. 1. Optical cavities that enhance the radiation pressure. (a) A symmetric Fabry-Perot cavity. The mirrors M_1 and M_2 are two identical slabs with thickness t separated by d. (b) An asymmetric Fabry-Perot cavity. M_1 is a slab with thickness t and M_2 is a semi-infinite mirror placed d away from M_1. (c) A nanostructured slot cavity array in a metal. (d) Profile of the nanostructured slot cavity in (c). A normally-incident plane wave of wavelength 633 nm and Au with artificially adjusted loss are assumed, as described in Table I.

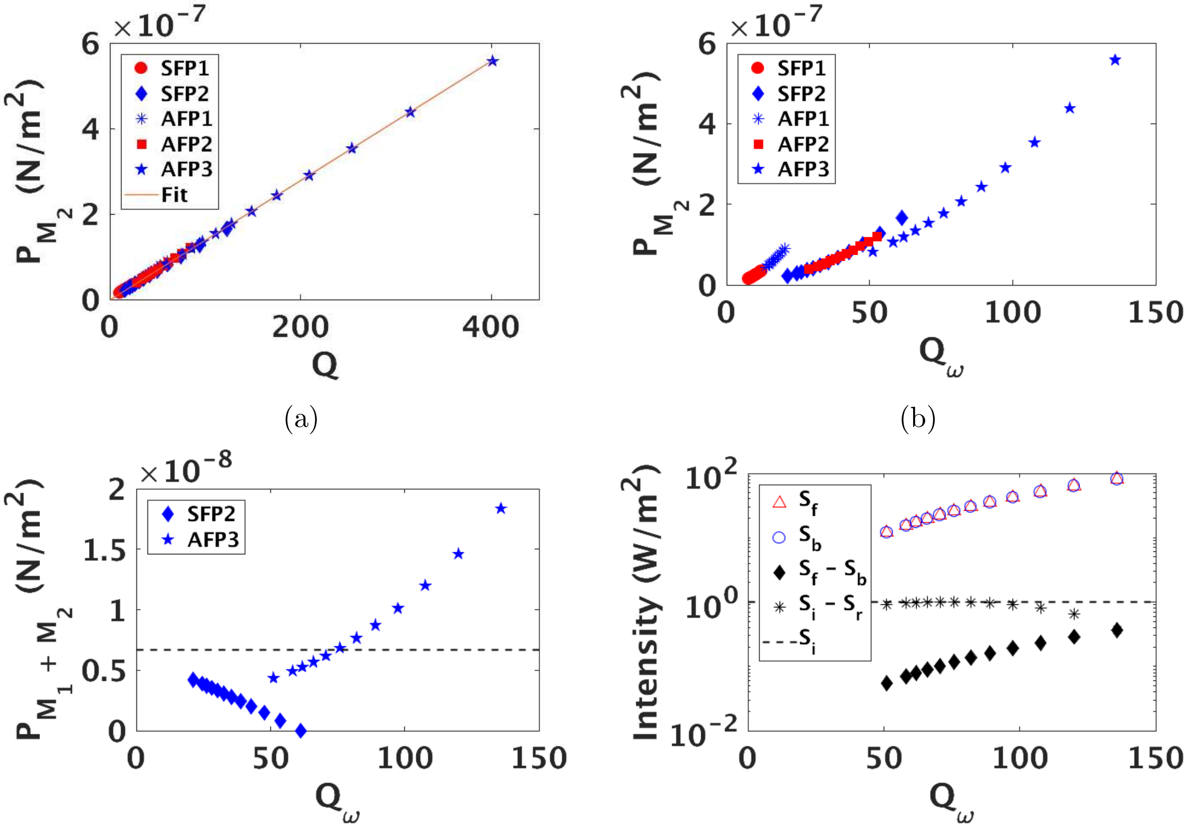

(a)

(b)

(c)

(d)

FIG. 2. (a) P_{M_2} on M$_2$ as a function of Q from (5), with a linear fit (orange line) for examples of symmetric and asymmetric Fabry-Perot cavities with the parameters given in Table I. (b) P_{M_2} as a function of Q_ω from (8). (c) Net pressure, $P_{M_1+M_2}$, on M$_1$ and M$_2$ as a function of Q_ω. The dashed line shows the value of the maximum pressure on a perfect mirror when the magnitude of the incident power density (S_i) is 1 W/m^2. A resonant asymmetric cavity can support larger pressure enhancement than a perfect reflecting (anti-resonant) surface. (d) Forward (S_f) and backward (S_b) power density for the asymmetric cavity AFP3 (overlapping on this scale), along with the difference ($S_f - S_b$), in comparison with the incident (S_i) and the net incident ($S_i - S_r$) power densities. As Q increases due to reduced loss in M$_1$, $S_f - S_b$ approaches $S_i - S_b$. This result establishes conservation of energy.

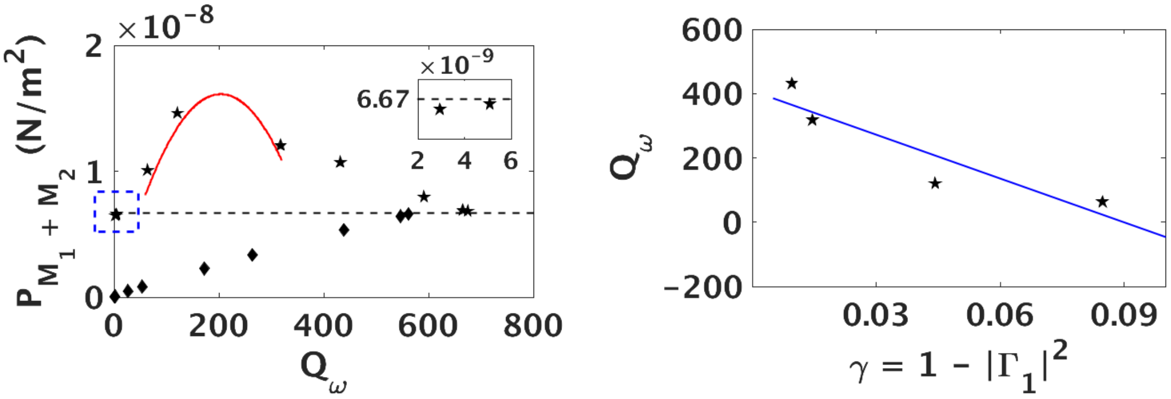

(a)

(b)

FIG. 3. (a) The net pressure on M_1 and M_2, $P_{\mathrm{M}_1+\mathrm{M}_2}$, as a function of Q_ω for symmetric (diamonds) and asymmetric (stars) Fabry-Perot cavities having $\epsilon'_{\mathrm{M1}} = \epsilon'_{\mathrm{M2}} = -11.82$ and $\epsilon''_{\mathrm{M1}} = \epsilon''_{\mathrm{M2}} = 0.1$. We choose the thickness of M_1, t, to be $5, 10, 40, 50, 70, 80, 100, 130$ and 150 nm to regulate the cavity quality factor, Q_ω, in the regime where enhancement occurs and beyond. The sub-figure shows an expanded view of the dashed box region for small Q_ω. The dashed line shows the value of the maximum pressure on a perfect mirror when the magnitude of the incident power density (S_i) is 1 $\mathrm{W/m^2}$, that used for the data points shown. For the symmetric cavities (diamonds), the total pressure increases with increasing Q_ω, and then approaches the perfect mirror case. For the asymmetric cavities (stars), note that the total pressure dips below that for S_i incident on a perfect mirror for low Q_ω. These results show that there is a design region for pressure enhancement. When t becomes large, the cavity behaves more like a symmetric cavity where the pressures on M_1 and M_2, due to S_b and S_f, approximately cancel. In this regime, the net pressure is roughly that from the excitation wave on a planar surface. The red parabola is from the local linear estimation for the asymmetric cavity data points with $t = 40, 50, 70$ and 80 nm and use of (16). (b) Calculated $Q_\omega(\gamma)$ with $\gamma = 1 - |\Gamma_1|^2$ (asymmetric cavity data points with $t = 40, 50, 70, 80$ nm). The blue line is a fit to all points, yielding $Q_\omega(\gamma) = a_n\gamma + b_n$ with $a_n = -4.5350 \times 10^3$ and $b_n = 407.3813$. With use of the point with $t = 50$ nm, which shows the largest enhancement in (a). and the corresponding Q (blue star symbol with the second largest Q for AFP3) in Fig. 2(a), we find $Q = \beta Q_\omega$ with $\beta = 2.6073$. The a_n and b_n provide local a and b values in (16) and the resulting parabolic curve in (a). Note how well this local, linear picture (the red parabola) captures the pressure enhancement.

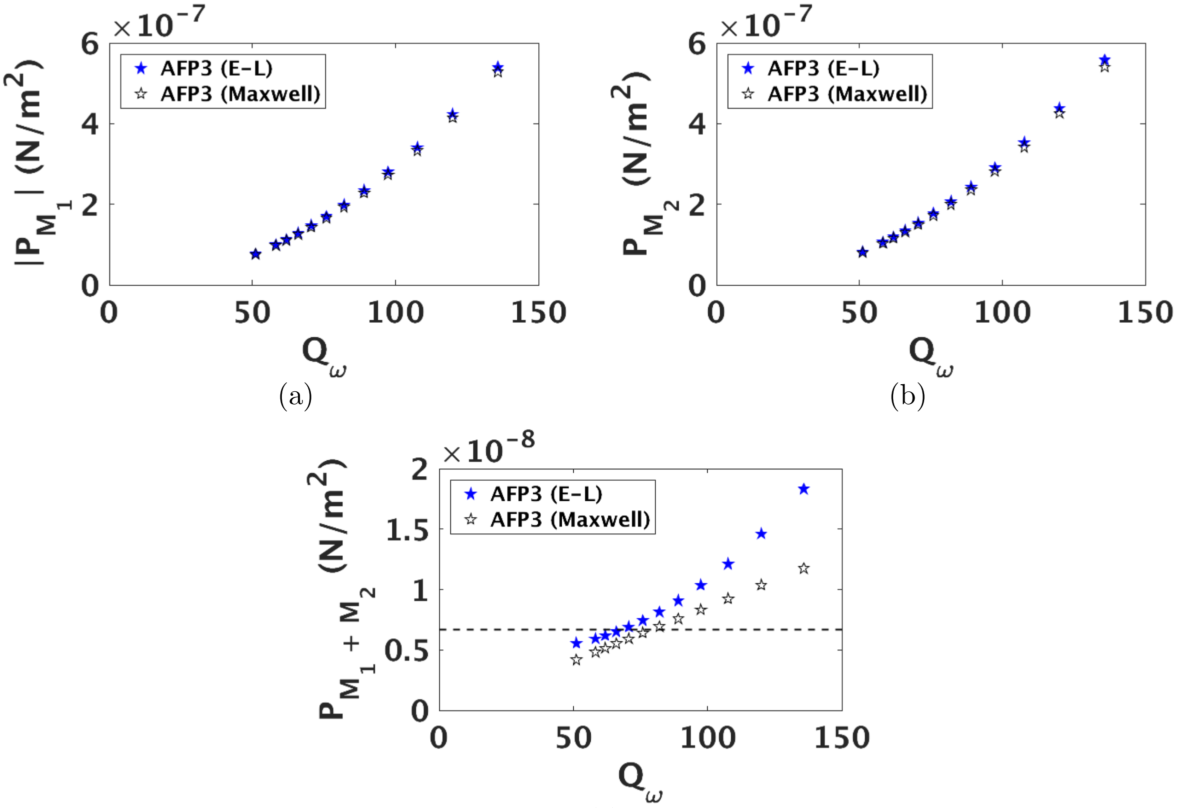

(a) (b)

(c)

FIG. 4. The pressures on M_1 and M_2 in the cavity of Fig. 1(b) using the Einstein-Laub (2) and Maxwell (1) descriptions, with varying loss for M_1 (ϵ''_{M1}) and hence varying cavity quality factor, Q_ω. $\epsilon'_{\mathrm{M1}} = \epsilon'_{\mathrm{M2}} = -11.82$ is fixed for both mirrors and $\epsilon''_{\mathrm{M2}} = 0.1$. (a) Radiation pressure on M_1 in Fig. 1(b), $|P_{M_1}|$, as a function of cavity quality factor, Q_ω, for the asymmetric Fabry-Perot cavity having mirror M_1 material properties described as AFP3 in Table I. Varying the mirror material causes Q_ω to change and hence the pressure, and this relationship is presented. The black stars are estimated from Maxwell's picture in (1), assuming there is no transmission through the mirror. The blue star symbols are calculated from the integral of the force density within the scattering material using the Einstein-Laub description in (2). (b) P_{M_2} from Maxwell's picture in (1) (black stars) and from the Einstein-Laub force density description in (2) (blue stars). (c) The net pressure, $P_{\mathrm{M}_1+\mathrm{M}_2}$, from Maxwell's picture in (1) (black stars) and from the Einstein-Laub force density description in (2) (blue stars). The larger differences with increasing Q_ω between the two approaches comes from the assumption of no transmission for M_1. The dashed line shows the value of the maximum pressure on a perfect mirror when the magnitude of the incident power density is 1 W/m^2. The enhanced pressure can be observed in both approaches. Our conclusion is that both theories present essentially the same mirror pressure results.

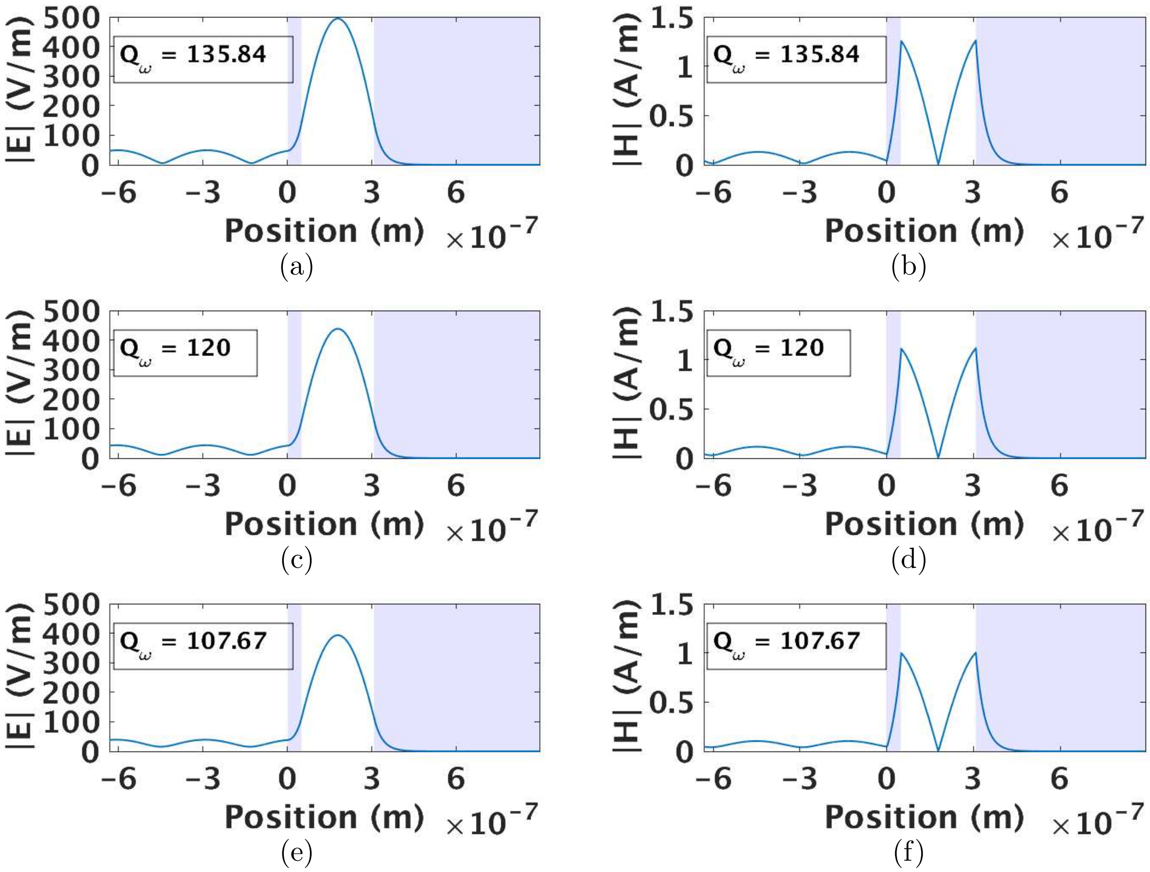

FIG. 5. Calculated analytical fields in the asymmetric 1D cavity as a function of propagation distance for the three AFP3 examples with the largest Q ($Q_\omega = 135.84, 120, 107.67$ when $\epsilon''_{\mathrm{M}_1} = 0, 0.1, 0.2$, respectively) in Fig. 4. (a) Magnitude of the electric field and (b) magnitude of the magnetic field as a function of axial position through the cavity and the mirror regions for $\epsilon''_{\mathrm{M}_1} = 0$. The shaded area indicates the positions of M_1 and M_2. (c) Magnitude of the electric field and (d) magnitude of the magnetic field as a function of axial position for $\epsilon''_{\mathrm{M}_1} = 0.1$. (e) Magnitude of the electric field and (f) magnitude of the magnetic field as a function of axial position for $\epsilon''_{\mathrm{M}_1} = 0.2$. The fields satisfy the boundary conditions and represent the unique solutions for first resonance that is used to produce the corresponding data points in Fig. 4. From Fig. 2(d), with $S_{\mathrm{i}} = 1$ W/m^2, for $\epsilon''_{\mathrm{M}_1} = 0$, $S_{\mathrm{f}} = 81.17$ W/m^2, $S_{\mathrm{b}} = 80.80$ W/m^2 and $|\Gamma_1|^2 = 0.9610$ ($Q_\omega = 135.84$); for $\epsilon''_{\mathrm{M}_1} = 0.1$, $S_{\mathrm{f}} = 63.8$ W/m^2, $S_{\mathrm{b}} = 63.51$ W/m^2 and $|\Gamma_1|^2 = 0.9557$ ($Q_\omega = 120$); for $\epsilon''_{\mathrm{M}_1} = 0.2$, $S_{\mathrm{f}} = 51.41$ W/m^2, $S_{\mathrm{b}} = 51.17$ W/m^2 and $|\Gamma_1|^2 = 0.9504$ ($Q_\omega = 107.67$). In all the cases, $|\Gamma_2|^2 = 0.9955$. The corresponding data points in Fig. 4(c) based on (1) are obtained with these numbers (at least to the approximation neglecting the pressure of the excitation light and transmission through M_1).

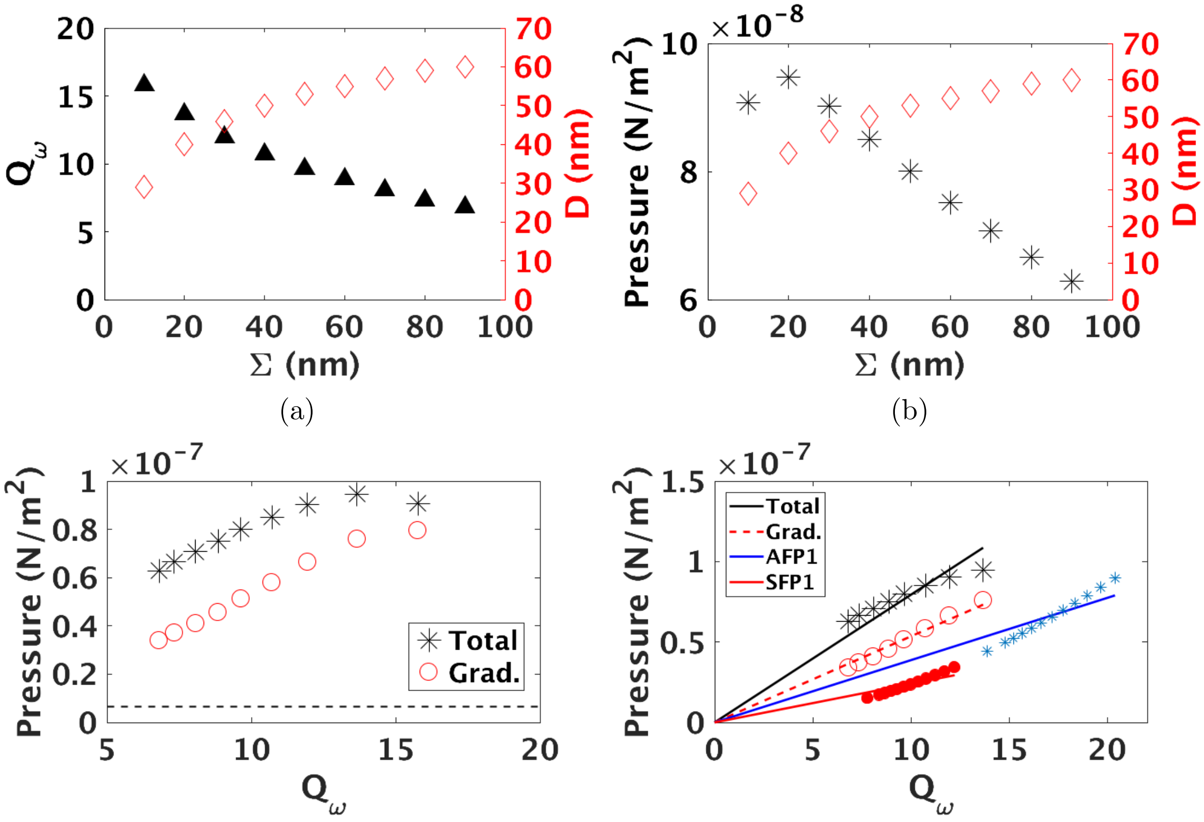

(a) (b)

(c) (d)

FIG. 6. Simulation results for the nanostructured slot cavity array in Au, and with reference to Fig. 1(d): $\Lambda = 400$ nm, $T = 200$ nm, Σ is fixed, and D is varied to determine the resonant depth D from the minimum of $|S_{11}|$. (a) Q_ω (triangles) and resonant slot depth, D (diamonds), as a function of slot width, Σ. (b) Radiation pressure (asterisks) along with the resonant D (diamonds) as a function of Σ. In general, smaller Σ results in higher Q_ω and larger pressure, consistent with the asymmetric 1D Fabry-Perot cavity results of Fig. 2(d), AFP3. (c) Radiation pressure as a function of Q_ω, decomposed into total and gradient ($\langle \mathbf{f_G} \rangle$) contributions. The dashed line shows the maximum pressure on a perfect mirror. The nanostructured slot cavity supports a pressure enhancement more than an order of magnitude higher than a perfect mirror. (d) Radiation pressure as a function of Q_ω for the lower Q 1D cavities, from Fig. 2, in comparison with the slot pressures from (c). The black line and red dashed line are the linear fits to the total pressure and $\langle \mathbf{f_G} \rangle$, respectively from the first 8 points in (c). The blue and red lines are the linear fits to P_{M2} for AFP1 and SFP1, which are low-Q Fabry-Perot cavities in the examples considered. The nanostructured slot cavity is more efficient in delivering radiation pressure enhancement on a target surface than the 1D Fabry-Perot cavity when the cavities have the same Q.

TABLES

	t_{M_1}	ϵ''_{M_1}	t_{M_2}	ϵ''_{M_2}
SFP1	30 nm	0, 0.1, 0.2, $\cdots$, 1 and 1.23 ($\Im\{\epsilon_{Au}\}$)	Same as M_1	
SFP2	50 nm			
AFP1	30 nm		Semi-infinite	1.23 ($\Im\{\epsilon_{Au}\}$)
AFP2	50 nm			
AFP3	50 nm			0.1

TABLE I. The cavity mirror material parameters used in the calculations related to Figs. 1(a) and (b). Nomenclature: symmetric Fabry-Perot (SFP), cases 1 (SFP1) and 2 (SFP2), as in Fig. 1(a); asymmetric Fabry-Perot (AFP), cases 1-3, as in Fig. 1(b). The dielectric constant assumed for Au is $\epsilon_{Au} = -11.82 + i1.23$ at a wavelength of 633 nm, and in all cases, $\epsilon'_{\mathrm{M1}} = \epsilon'_{\mathrm{M2}} = -11.82$. The imaginary part of the dielectric constant for each mirror, ϵ''_{M1} and ϵ''_{M2}, is varied as indicated to adjust the confinement and dissipation in the cavities.